Novel magnetically separable of $Fe_3O_4/Ag_3PO_4@WO_3$ nanocomposites for enhanced photocatalytic and antibacterial activity against *Staphylococcus aureus* (*S. aureus*)

Hind Baballa Gasmalla[1,2], Xiaoquan Lu[3], Mahgoub Ibrahim Shinger[4], Lubin Ni[1], Aadil Nabi Chishti[1] and Guowang Diao[1*]

Abstract

Background: Iron oxide nanocomposites have received a great attention for their application in various fields like physics, medicine, biology, and material science etc., due to their unique properties, such as magnetism, electrical properties, small size, biocompatibility and low toxicity.

Methods: $Fe_3O_4/Ag_3PO_4@WO_3$ nanocomposites with different weight percent of Ag_3PO_4 were successfully prepared through fabricated Ag_3PO_4/Fe_3O_4 with WO_3 via in situ fabrication method, electrospinning involved precursor solution preparation and spinning to enhance photocatalyst performance under simulated sunlight for the degradation of methylene blue (MB) and antibacterial activity against *Staphylococcus aureus* (*S. aureus*).

Results: The photocatalytic degradation of methylene blue (MB) under simulated light irradiation indicated that the nanocomposite with 0.25 mg of Ag_3PO_4 has the best activity. An additional advantage of these photocatalysts is magnetic recoverability, using external magnetic field and photocatalytic stability of the nanocomposites was evaluated for three cycles. In addition, using different scavengers, holes (h^+) and superoxide radical ($O_2^{\cdot-}$) radicals and hydroxide radical ($\cdot OH$) were identified the main oxidative species in the degradation reaction of methylene blue.

Conclusions: The results reveal that $Fe_3O_4/Ag_3PO_4@WO_3$-0.25 nanocomposites have photocatalytic and antibacterial activity against *S. aureus*. The photocatalyst and mechanism based on the enhancement of electron transfer processes between Ag_3PO_4 and WO_3 nanoparticles.

Keywords: $Fe_3O_4/Ag_3PO_4@WO_3$, Photocatalyst, Simulated light irradiation, Antibacterial activity

Introduction

In recent years, research attention has been focused on processes that lead to an improved oxidative degradation of organic pollutants. Therefore, semiconductor photocatalysis technology has aroused scientists' interest in environmental remediation. Although several semiconductors have proven to be ideal candidates for

the treatment of water pollution, the efficient separation and recycling of this fine powdered photocatalyst is still a scientific problem when applied in practice, including separation process, selectivity, and dispersion [1, 2]. A photocatalyst with magnetic properties allow the use of the technique of magnetic separation, which is one of the most effective and simple methods for removing suspended solids from wastewater without need for further separation processes. The magnetic photocatalyst allows its use as a suspended material and providing the advantage to have a high surface area for reaction [3]. Several complexes such as Fe_2O_3, WO_3, $BiVO_4$, Bi_2WO_6 and Ag_3PO_4 [4–8] have been tested as visible

*Correspondence: gwdiao@yzu.edu.cn; hindbibo@yahoo.com
[1] Key Laboratory of Environmental Materials & Environmental Engineering of Jiangsu Province, College of Chemistry and Chemistry Engineering, Yangzhou University, Yangzhou 225002, China
Full list of author information is available at the end of the article

Gasmalla *et al. J Nanobiotechnol* (2019) 17:58

Page 2 of 14

light photocatalyst. Fe_3O_4 has been broadly applied as a significant ferromagnetic material for extensive application areas, including catalysis, recording materials, pigment, magnetocaloric refrigeration, and drug delivery carrier, because of its promising properties such as low cost, good hydrophilicity, and biocompatible properties [4]. Although Fe_3O_4 is not a suitable semiconductor for the photocatalyst process, it wasn't expensive and possess high band gap energies as they willingly go through photocathodic corrosion [9, 10]. But the magnetic $Ag_3PO_4/TiO_2/Fe_3O_4$ heterostructured nanocomposite was enhanced photocatalytic activity, cycling stability, and long-term durability in the photodegradation of acid orange 7 (AO7) under visible light. Moreover, the antibacterial activity toward *Escherichia coli* (*E. coli*) cells under visible-light irradiation [11].

Ag_3PO_4 has a relatively narrow band gap (2.36–2.43 eV) and is thus active under visible-light irradiation ($\lambda < 530$ nm). Therefore, as a highly efficient photocatalyst, Ag_3PO_4 could behave as a potential antimicrobial material and could have promise in various antimicrobial applications [12, 13]. Magnetically separable composite photocatalysts Fe_3O_4–Ag_3PO_4 [14], $Ag_3PO_4/NiFe_2O_4$ [15] and $Fe_3O_4@LDH@Ag/Ag_3PO_4$ [16] with high photocatalytic activity. Recently, magnetic and silver phosphate core–shell photocatalysts composed of a magnetic core and photocatalytic shell have attracted great interest $Fe_3O_4@Ag_3PO_4/AgCl$ under simulated solar light [17] and $Fe_3O_4@SiO_2@Ag_3PO_4$ with excellent visible-light-responding photocatalytic activity [18]. WO_3 has a narrow band gap (2.6–2.7 eV), is very hopeful visible light active photocatalyst. It has been used in the photocatalytic degradation of organic contaminants and in the photocatalytic development of O_2 [19–21]. Micro and nanoscaled core–shell materials have attracted great interest because their essential properties can be conveniently adjusted by controlling the morphology and chemical composition of both core and shell [22–24]. Moreover, the interactions between the various ingredients of the core and shell can significantly improve the overall performance of the core–shell system and even produce beneficial synergistic effects [25, 26]. For example, metal–semiconductor as core–shell photocatalysts have been synthesized and shown to display superior photocatalytic efficiency, because a metallic core can accelerate charge separation and the large-surfaced nanostructures enhance light absorption [27]. However, the photocatalytic activity of WO_3 is not reasonable because of its relatively low conduction band level. There are some reports on the synthesis of chestnut, such as Fe_3O_4/WO_3 hierarchical core–shell structures that integrate conductive Fe_3O_4 microspheres and visible light active WO_3 nanoplates as a magnetically recyclable

visible light active photocatalyst [27]. In another study the fabrication of a magnetically recyclable Fe_3O_4/WO_3 core–shell visible-light photocatalyst has been developed [28]. Nanosilver-decorated WO_3 nanofibers incorporating paramagnetic $CoFe_2O_4$ nanoparticles were fabricated for the first time as model solar light-active photocatalyst with potent antibacterial property and recoverability. Formation of semiconductor composites is an effective way to enhance the photo-induced charges separation efficiency and the photocatalytic performance, which has been extensively studied for the last decades [20].

Magnetic photocatalysts are recognized as low cost, efficient, and robust techniques desirable to remove dyes from contaminated water before their discharge and to produce clean water on a large scale. In principle, the rapid separation of photogenerated electrons and holes can be achieved by forming heterojunctions within the semiconductors. Further, multiscale structuring can beneficially increase the light scattering and absorption in such heterojunctions, thus increasing the light absorption range [29]. Hence, such a strategy can be successfully used for the fabrication of high-efficiency semiconductor composites.

In the present work, through in situ ion exchange method, we fabricated Ag_3PO_4/Fe_3O_4 with WO_3 for the first time as model simulated light-active photocatalyst for the degradation of methylene blue (MB). The antibacterial activity of $Ag_3PO_4/Fe_3O_4@WO_3$ composite toward *Staphylococcus aureus* (*S. aureus*) was studied. The as synthesized $Ag_3PO_4/Fe_3O_4@WO_3$ composite exhibited high antibacterial performance than the other prepared composites. The effect of the presence of the reactive species on the photocatalytic activity was studied, and the possible photocatalytic mechanism of $Fe_3O_4/Ag_3PO_4@WO_3$ and photodegradation pathway of MB was suggested.

Experimental section
Materials
All materials have analytical purity and used as received without further purification. All of the solutions were prepared using deionized water (18.2 MΩ). $FeSO_4 \cdot 7H_2O$, $FeCl_3 \cdot 6H_2O$, NH_4OH and Disodium ethylenediamine tetraacetate (Na_2-EDTA) solution were obtained from Yantai both chemical Co., Ltd, $AgNO_3$ (99.8%), MDF and *p*-benzoquinone (BZQ) were obtained from Tianjin Chemical reagent technology Co., Ltd. Disodium hydrogen phosphate dodecahydrate ($Na_2HPO_4 \cdot 12H_2O$) and H_2WO_4 (AR, 99.95%) was bought from Aladdin reagent Co., Ltd., Ethanol (AR, 99.7%), was purchased from Tianjin Baishi Chemical Co., Ltd. PVP, MB and tert-butanol obtained from Tianjin city Tianxin chemicals development center, Nutrient Broth powder was obtained from

Gasmalla *et al. J Nanobiotechnol*   (2019) 17:58

Page 3 of 14

Hanzhou Microbiology Co., Ltd and agar powder was obtained from Beijing life science and technology. Co., Ltd.

Preparation Fe_3O_4 nanoparticles

The functionalized Fe_3O_4 was prepared by the modified co-precipitation method. Typically, 2.7 g $FeSO_4 \cdot 7H_2O$ and 5.4 g $FeCl_3 \cdot 6H_2O$ were dissolved in 50 ml deionized water separately, and mixed together in water bath maintained at 80 °C. Then 2 ml of oleic acid (OA) was added into the $FeSO_4/FeCl_3$ mixture, and sonicated for 20 min under 60 °C, then 15 ml of ammonium hydroxide was added drop by drop with stirring (600 revolutions/min) under nitrogen atmosphere. After 0.5 h, 2 ml of OA was added again drop-by-drop to the mixture with stirring and reacted for 1 h at 80 °C under nitrogen gas. After that, the precipitate was isolated from the solvent by a permanent magnet. Then washed with water and ethanol in sequence, followed by drying at 50 °C under vacuum for 24 h. Non-functionalized Fe_3O_4 was prepared following the same method without the addition of OA, and labeled as Fe_3O_4-non.

Preparation of Fe_3O_4/Ag_3PO_4

For the preparation of Fe_3O_4/Ag_3PO_4, room temperature in situ anion-exchange method was used. Typically, 0.5 g of the as prepared Fe_3O_4 was dispersed into 50 ml distilled water and sonicated for 1 h to give black aqueous suspension and then 10 ml of three different amount of $AgNO_3$ (0.25 g, 0.50 g and 0.75 g) was added into the suspension solution and stirred for 0.5 h. Subsequently, 10 ml of aqueous solution with different content of Na_2HPO_4 (0.13 g, 0.26 g, 0.39 g) was added drop-by-drop with continues stirring for more 0.5 h. Finally, the precipitates were separated by a permanent magnet and washed with distilled water several time and dried under vacuum for 24 h. The obtained composites were labeled as Fe_3O_4/Ag_3PO_4-0.25, Fe_3O_4/Ag_3PO_4-0.5 and Fe_3O_4/Ag_3PO_4-0.75. Fe_3O_4/Ag_3PO_4-non was prepared using Fe_3O_4-non and (0.25 g/10 ml) $AgNO_3$ and (0.13 g/10 ml) Na_2HPO_4.

Preparation of tungsten oxide WO_3

Fabrication of WO_3 square like nanoplates by electrospinning involved precursor solution preparation and spinning. Combination of a polymer solution and a tungsten oxide precursor solution resulted in precursor gel for electrospinning. The polymer solution could be prepared by dissolving a selected polymer in a solvent while the tungsten oxide precursor solution by dissolving the salt in a suitable solvent. The following protocol is given as a specific example; A PVP solution was prepared by adding 0.7 g of polyvinylpyrrolidone into 7 ml of ethanol under magnetic stirring. In a separate beaker, 0.2 g of tungstic

acid was added to 2 ml of DMF. Then, the two solutions were mixed followed by magnetic stirring at room temperature for 15 min. Then the precipitates were separated by a permanent magnet and washed with distilled water several time and dried under vacuum for 24 h.

Preparation of $Fe_3O_4/Ag_3PO_4@WO_3$

The fabrication of magnetic with silver phosphate involved WO_3 precursor solution preparation and electrospinning was chosen as a facile and an effective approach to fabricate plates with diameters at nanometer length scale. The precursor solutions were derived from mixtures Fe_3O_4/Ag_3PO_4 nanoparticles with different concentration and tungsten oxide precursor. A typical method is as follows. A PVP solution was prepared by adding 0.7 g of polyvinylpyrrolidone into 7 ml of ethanol under magnetic stirring. In a separate beaker, 0.2 g of tungsten acid was added to 2 ml of DMF. Then, the two solutions were mixed followed by magnetic stirring at room temperature for 15 min. To the mixture above, determined about 0.1 mg of different amounts of $Fe_3O_4@Ag_3PO_4$ nanoparticles were added. The final mixture was then stirred by a magnetic stirrer at room temperature for 15 min, followed by sonication for 10 min. Then the precipitates were separated by a permanent magnet and washed with distilled water several time and dried under vacuum for 24 h. The obtained composites were labeled as $Fe_3O_4/Ag_3PO_4@WO_3$-0.25, $Fe_3O_4/Ag_3PO_4@WO_3$-0.05 and $Fe_3O_4/Ag_3PO_4@WO_3$-0.75. Non-functionalized $Fe_3O_4/Ag_3PO_4@WO_3$ was synthesized by the same method using Fe_3O_4/Ag_3PO_4-non instead of Fe_3O_4/Ag_3PO_4, and labeled as $Fe_3O_4/Ag_3PO_4@WO_3$-non.

Characterization

The morphology and the composition were characterized; Transmission Electron Microscopy (TEM, FEI TECNAI-G2 operating at 300 kV) and Field-emission Scanning Electron Microscope (FESEM, JEOL, JSM-7001F) were used to determine the morphology and size of the magnetite particles, The structures of composites were characterized by X-ray diffractometer (XRD) using a Brucker 8 Advanced, Germany with a Cu Kα ($\lambda = 1.5406°$ A) source in the 2θ range of 10° to 80° at room temperature, A vibration sample magnetometer VSM (Model EV9System) was employed for magnetic properties of the samples at room temperature, The Fourier Transform Infrared (FTIR) spectra of the samples were recorded on a Bruker Vertex 70 FT-IR spectrophotometer using the KBr method, The UV–visible diffuse reflectance spectroscopy (DRS) spectra of photocatalyst powder was obtained for the dry-pressed disk samples using scan Shimazu, Japan UV-2450 spectrometer equipped with the integrated sphere accessory for diffuse

reflectance spectra, using $BaSO_4$ as the reflectance sample, UV–vis absorption spectra of the as-prepared samples were obtained using a Hitachi U-4500 spectrophotometer (Hitachi High-Technology Corporation). The electron transfer properties of the synthesized composites were studied using electrochemical impedance spectrometer (EIS) VMP2 multi-potentiostat with ZsimpWin program (Princeton Applied Research, USA) and it's frequencies swept from 10 kHz to 100 mHz.

Evaluation of the antibacterial activity
Preparation of photocatalyst film
In general, suspensions of the as-prepared Fe_3O_4/Ag_3PO_4@WO_3 composites (0.001 mg/1 ml) were dripped onto filter paper (Φ 6 mm), and then placed onto the bottom of a Petri dish (nutrient agar plate) for antibacterial experiments. For comparison, the same film was prepared using Fe_3O_4, Ag_3PO_4 or WO_3.

Antibacterial tests
The antibacterial activity was evaluated using *S. aureus* and *E. coli* as representative microorganisms. Before the antimicrobial experiments, all glass wares were sterilized by autoclaving at 120 °C for 30 min. To measure antibacterial activity, 100 µl of the bacterial suspension was serially diluted with sterile water to make sure the final colony count is not more than 10^{-7} colony-forming units per milliliter ($CFU\ ml^{-1}$). Then 100 µl aliquots were spread onto nutrient agar plates that were prepared already and incubated at 37 °C for 24 h. The experiment was further repeated. For each antibacterial experiment, the prepared photocatalyst film was placed onto the bottom of a Petri dish (onto an agar plate) seeded with 100 µl of *S. aureus* or *E. coli*. After 24 h of incubation at 37 °C, the diameters of the inhibition zones were measured.

Photocatalytic activity
The photocatalytic evaluation study was carried out at room temperature. Typically, MB solution (50 ml, 5 mg l^{-1}) and 15 mg of the catalyst were placed in a sealed glass. The suspension was ultrasonicated in the dark for 10 min before irradiation to reach an adsorption/desorption equilibrium between MB and the surface of the catalyst under room temperature. Then the mixture was illuminated with 350 Xe lamp as a light source system equipped with a UV cutoff filter ($\lambda > 420$ nm). The distance between the light source and the reaction containers was fixed at 10 cm. After simulated light irritation, 3 ml of the mixture was taken out at a regular time interval of 1 min. Then centrifuged to remove the photocatalyst and the concentration of MB was measured with UV–Vis spectrophotometer at 664 nm.

Analysis of hydroxyl radical (˙OH)
Terephthalic acid photoluminescence probe technique was used in the detection of ˙OH. Terephthalic acid readily reacted with OH to produce highly fluorescent product, 2-hydroxy-terephthalic acid. The method relied on the PL signal at 426 nm of 2-hydroxyterephthalic acid. The PL intensity of 2-hydroxyterephthalic acid was proportional to the amount of ˙OH formed. Experimental procedures were reported in early reports [30, 31], a basic terephthalic acid solution was added to the reactor and the concentration of terephthalic acid was set at 5×10^{-4} M in 2×10^{-3} M NaOH solution. The solution was irradiated for intervals time 10 min using ultraviolet light 365 for 50 min under magnetic stirring. The PL spectra of generated 2-hydroxyterephthalic acid were measured on a Hitachi F-4500 fluorescence spectrophotometer. The reaction solution was used to measure the increase of the PL intensity at 426 nm excited by 365 nm ultraviolet light.

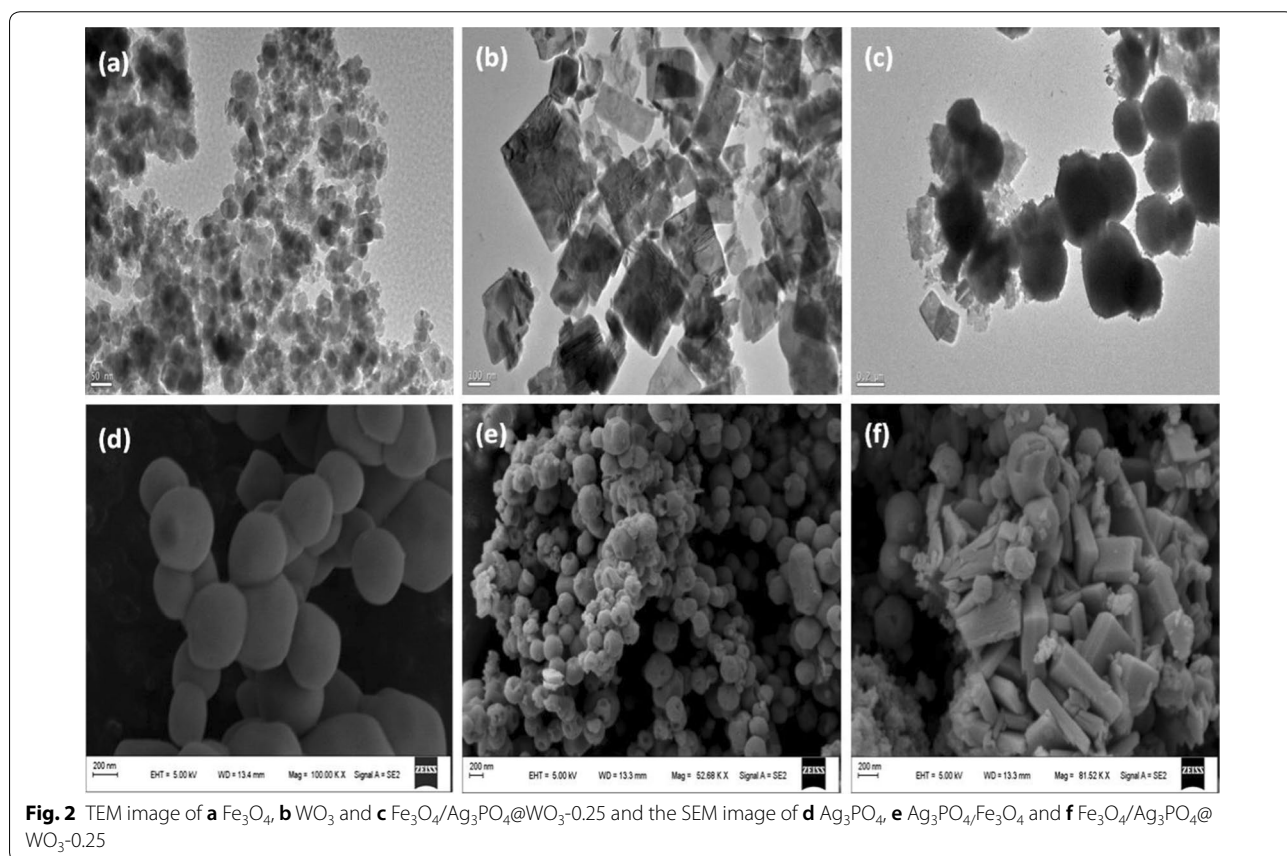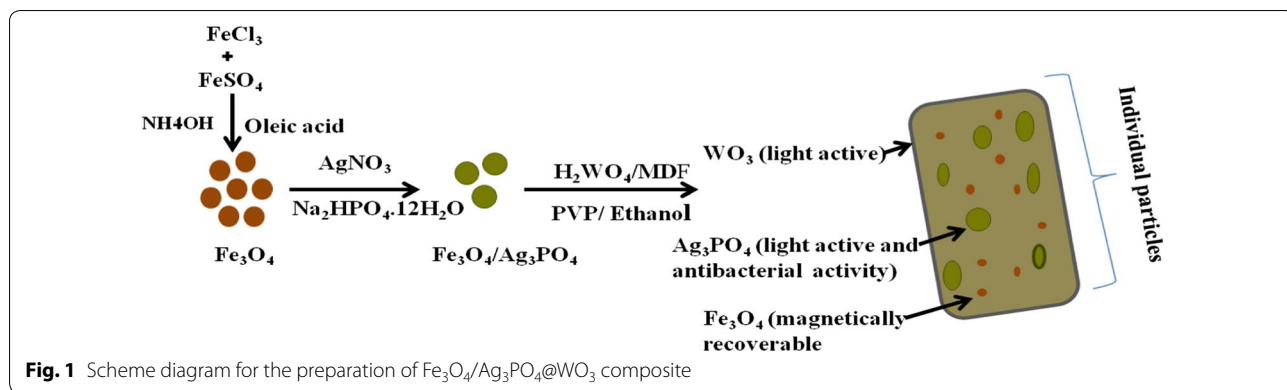## Result and discussion
Characterization
Transmission electron microscopy
This synthesis procedure of Fe_3O_4/Ag_3PO_4@WO_3 nanocomposites is presented Schematic diagram in Fig. 1. A Fe_3O_4 nanoparticle was first synthesized by co-precipitation method and fabrication of magnetic with silver phosphate involved WO_3 precursor solution preparation and electrospinning method.

Figure 2a–c presents typical TEM images of the bare Fe_3O_4, Ag_3PO_4 and WO_3, Fe_3O_4/Ag_3PO_4@WO_3 composites, respectively. As seen in Fig. 2c, the as prepared Fe_3O_4/Ag_3PO_4 well cabled with the WO_3 nanoplates, indicating the Fe_3O_4/Ag_3PO_4@WO_3 composite has been successfully fabricated spherical shape with wide size distribution, and the aggregation of the particles is dense and the size range of bare Fe_3O_4 nanoparticles is 29 nm Fig. 2d–f shows the SEM images of the Ag_3PO_4, Fe_3O_4/Ag_3PO_4, and Fe_3O_4/Ag_3PO_4@WO_3 composites, respectively. As been seen in (Fig. 2e), the Fe_3O_4 nanoparticles obviously decorated the Ag_3PO_4. While the SEM image of the Fe_3O_4/Ag_3PO_4@WO_3 shows the presence of Fe_3O_4, Ag_3PO_4 and WO_3. Which further confirm the fabrication of Fe_3O_4/Ag_3PO_4@WO_3.

X-Ray energy-dispersive spectroscopy analysis
The purity of the samples was investigated using EDS analysis and the results are shown in Fig. 3a. As can be seen the peaks in the spectra of the Fe_3O_4/Ag_3PO_4@WO_3-0.25 composite are described to O, W, P, Fe, and Ag elements. Moreover, the EDS elemental mapping further elucidated the composition of the Fe_3O_4/Ag_3PO_4@

Gasmalla *et al. J Nanobiotechnol*   (2019) 17:58

Page 5 of 14

Fig. 1 Scheme diagram for the preparation of $Fe_3O_4/Ag_3PO_4@WO_3$ composite

Fig. 2 TEM image of **a** Fe_3O_4, **b** WO_3 and **c** $Fe_3O_4/Ag_3PO_4@WO_3$-0.25 and the SEM image of **d** Ag_3PO_4, **e** Ag_3PO_4/Fe_3O_4 and **f** $Fe_3O_4/Ag_3PO_4@$ WO_3-0.25

WO_3-0.25 nanocomposite. As can be seen in Fig. 3b–g, the elemental mapping images of O, W, P, Fe and Ag have similar shape and location, indicating the definite existence of Fe_3O_4, Ag_3PO_4, and WO_3.

X-ray diffraction

The XRD analysis was used to investigate the different crystalline structures of the synthesized composites (Fig. 4). The Fe_3O_4 shows six characteristic peaks at

$2\theta = 30.1, 35.3, 43.6, 53.6, 57.3$ and 62.8, indexed to (220), (311), (400), (422), (511) and (440) facets, respectively, which can be well indexed to the standard data (JCPDS File, no: 19-0629) [32]. The XRD pattern of Ag_3PO_4 shows diffraction peaks at $2\theta = 20.848, 29.648, 33.248, 36.518, 42.428, 47.718, 52.608, 54.928, 57.188, 61.548, 65.728, 69.788, 71.768,$ and 73.728 corresponded to the planes (110), (200), (210), (211), (220), (310), (222), (320), (321), (400), (330), (420), (421) and (332) of Ag_3PO_4,

Gasmalla *et al. J Nanobiotechnol*   (2019) 17:58

Page 6 of 14
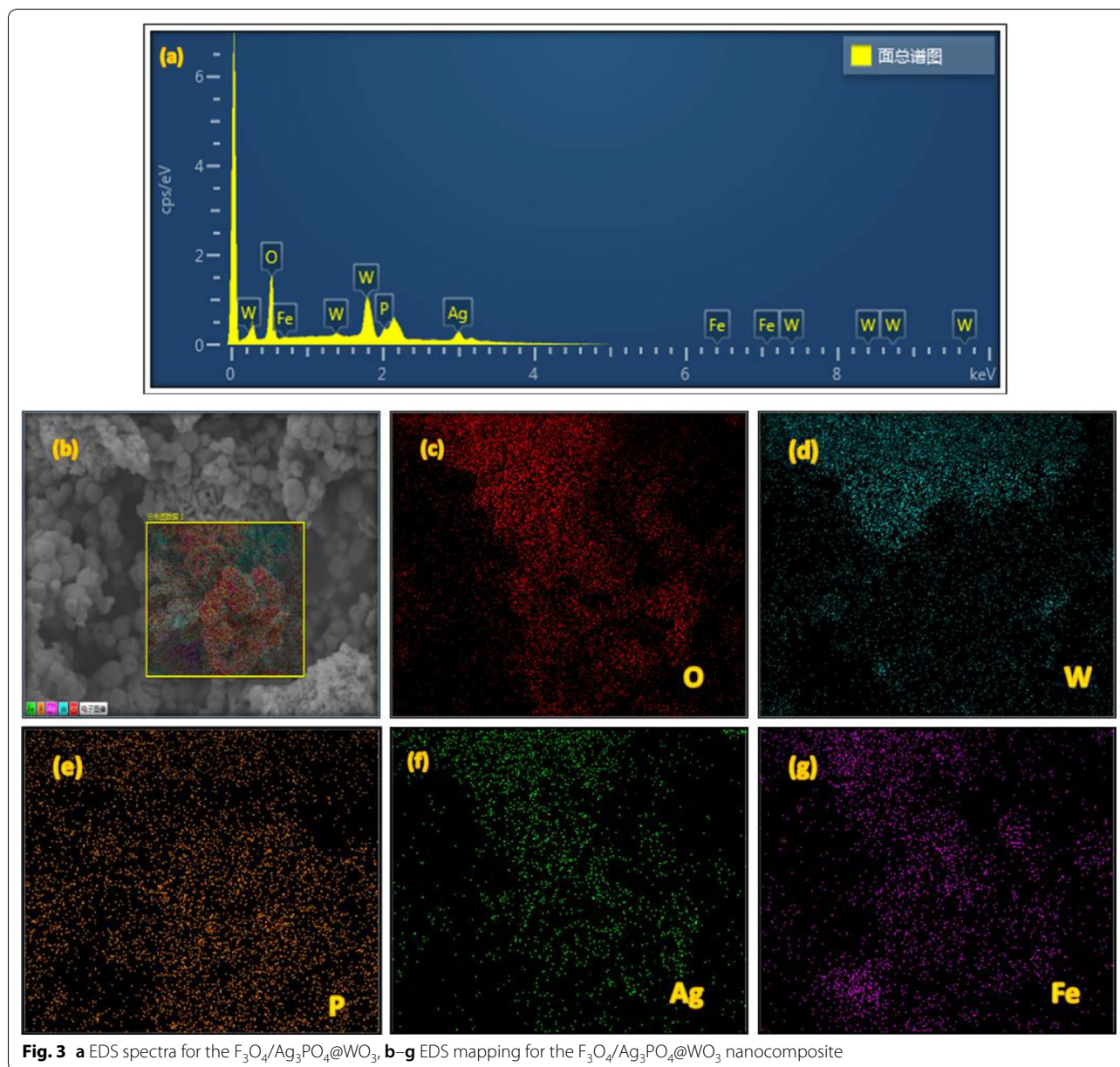
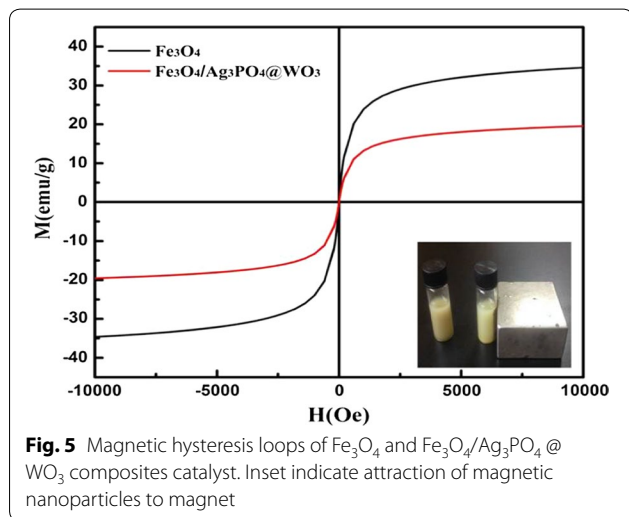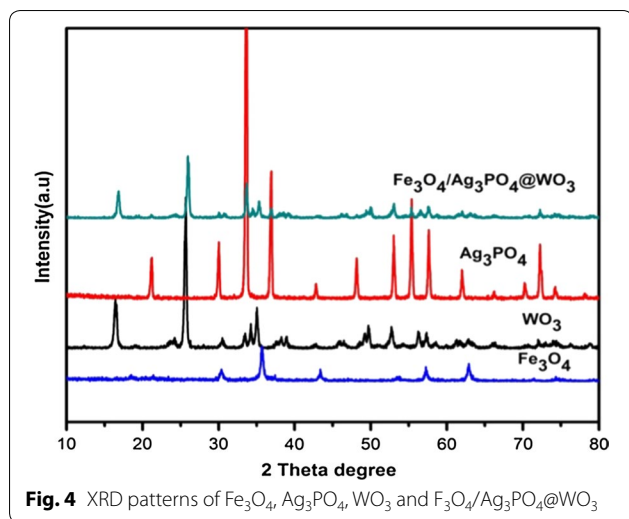**Fig. 3 a** EDS spectra for the F$_3$O$_4$/Ag$_3$PO$_4$@WO$_3$, **b–g** EDS mapping for the F$_3$O$_4$/Ag$_3$PO$_4$@WO$_3$ nanocomposite

respectively, which can be indexed to the standard XRD data of the cubic-phase Ag$_3$PO$_4$ crystal (JCPDS File, no: 06-0505, 74-1876) [33, 34]. The square-like WO$_3$ nanoplates indicate that the as-synthesized WO$_3$ crystal structure with obvious diffraction peaks at 2θ value of 16.5° (020), 19.2.8° (011), 23.8° (120), 25.8° (111), 35.5° (131), and 78.6° (313) which are similar to the pattern of the reference WO$_3$ crystals (JCPDS File no: 84-886) [35]. The XRD pattern of Fe$_3$O$_4$/Ag$_3$PO$_4$@WO$_3$ composite displayed all the characteristic peaks of Fe$_3$O$_4$, Ag$_3$PO$_4$ and WO$_3$, and no other peaks were detected. This further confirms the fabrication of the synthesized composite.

The particle size play important role on the photocatalytic performance of the semiconductors, the less particle sizes the higher catalytic activity. To calculate the particle size of the synthesized composites, Scherrer's Eq. 1 [36] was used.

$$D = K\lambda/\beta\cos\theta \tag{1}$$

where β is full width at half-maximum, D is crystallite size, λ is X-ray wavelength, θ is Bragg's diffraction angle.

The average sizes of the WO$_3$ were estimated to be 450, 411 and 383 corresponding to the patterns of Fe$_3$O$_4$/Ag$_3$PO$_4$ and Fe$_3$O$_4$/Ag$_3$PO$_4$@WO$_3$, respectively.

Gasmalla *et al. J Nanobiotechnol*   (2019) 17:58

Page 7 of 14

Fig. 4 XRD patterns of Fe_3O_4, Ag_3PO_4, WO_3 and $F_3O_4/Ag_3PO_4@WO_3$

Fig. 5 Magnetic hysteresis loops of Fe_3O_4 and $Fe_3O_4/Ag_3PO_4@WO_3$ composites catalyst. Inset indicate attraction of magnetic nanoparticles to magnet

From the calculations, the crystalline size of Fe_3O_4/Ag_3PO_4 markedly decreased after the synthesis of $Fe_3O_4/Ag_3PO_4@WO_3$ composite. Which it's beneficial enhance the photocatalytic activity.

Magnetic properties

The magnetic properties have been quantified by using a superconducting quantum interference device a vibrating sample magnetometer (VSM Model EV9System) at room temperature. Figure 5, displayed the hysteresis loops at 300 K of the as prepared Fe_3O_4 microspheres and $Fe_3O_4/Ag_3PO_4@WO_3$-0.25 composites catalysts. The saturation magnetization (Ms), remanence (Mr), coercivity (Hc) and loop Squarenses ratio (Mr/Ms) of samples is shown in (Tables 1 and 2) and the magnetization curve with a hysteresis loop displays ferromagnetic behavior with a coercivity of about 2.20 and 1.87Oe of Fe_3O_4 and $Fe_3O_4/Ag_3PO_4@WO_3$ respectively. The saturation magnetization of the $Fe_3O_4/Ag_3PO_4@WO_3$-0.25 composites is about 36.225 and 20.525 $emug^{-1}$ respectively. Such a decrease of their saturated magnetization could be attributed to the decrease in effective mass of the Fe_3O_4 in these cases. Fortunately, the magnetism of these hybrid nanostructures was still strong enough to be separated easily from solution with the help of an external magnetic field.

Fourier transforms infrared spectroscopy

The typical vibration peaks of the Fe_3O_4, Ag_3PO_4, WO_3, and $Fe_3O_4/Ag_3PO_4@WO_3$ composite are shown in the FT-IR spectrum in (Fig. 6). In the spectra of the functionalized Fe_3O_4, the presence of OA layer can be confirmed. The bands at 2840 cm^{-1} and 2917 cm^{-1} can be ascribed to the stretching modes of $-CH_2$ and $-CH_3$ of the OA, respectively. The vibrations at 1699 cm^{-1} and 1454 cm^{-1} can be assigned to the stretching modes of $-C=O$ and $-C=C-$ of the OA, respectively. The characteristic band of the pure Fe_3O_4 usually appears at 570 cm^{-1}, in the case of the present sample, this peak was shifted to 579 cm^{-1}, due to the functionalization process. In the spectra of Ag_3PO_4, the intense absorption peak at 1016 cm^{-1} is ascribed to the stretching vibration of the phosphate (PO_4^{3-}) group, and the absorption peaks at 574 and 538 cm^{-1} is ascribed to the bending vibration of the phosphate (PO_4^{3-}) group. The absorption peaks at 3450 and 1660 cm^{-1} are corresponding to the ^-OH stretching and bending vibrations of physically absorbed H_2O molecules, respectively. The precursor of WO_3 has strong

Table 1 Magnetic properties of Fe_3O_4

Parameter	Upward part	Downward part	Average	Hysteresis parameter
Mr (emu/)	0.2394	0.207125	0.223275	Remanent magnetization: M H = 0
S	0.007	0.006	0.006	Squarenses: Mr/Ms
S*	0.134	0.157	0.146	1 − (Mr/Hc)(1/slop at Hc)
Ms (emu/g)	36.225	36.2	36.225	Saturation magnetization: maximum M measure
Hc Oe	2.36	− 2.04	2.20	Coercive field: field at which M/H changes sign

Table 2 Magnetic properties of the $Fe_3O_4Ag_3PO_4@WO_3$

Parameter	Upward part	Downward part	Average	Hysteresis parameter
Mr (emu/)	0.0096	0.0084	0.0090	Remanent magnetization: M H = 0
S	0.005	0.004	0.003	Squarenses: Mr/Ms
S*	0.118	0.136	0.127	1 − (Mr/Hc)(1/slop at Hc)
Ms (emu/g)	20.520	20.53	20.525	Saturation magnetization: maximum M measure
Hc Oe	2.00	− 1.75	1.87	Coercive field: field at which M/H changes sign

Fig. 6 FTIR Spectrums of the WO_3, Fe_3O_4, $Fe_3O_4/Ag_3PO_4@WO_3$ and Ag_3PO_4, Composite
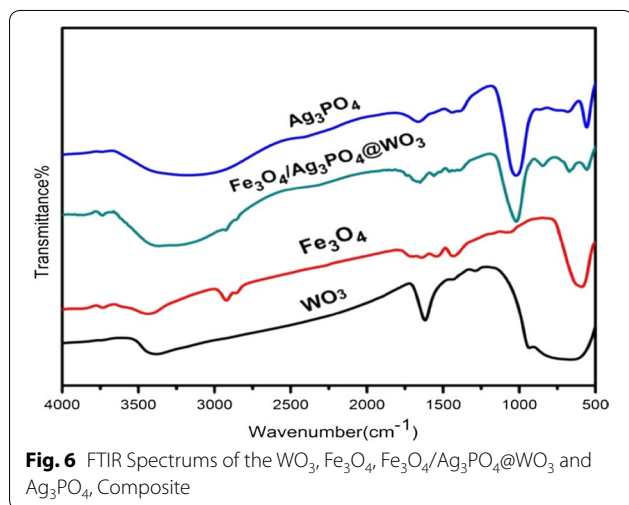
bands in the 500–900 cm^{-1} region are assigned to the ν(O–W–O) stretching mode [37]. A band at 950 cm^{-1} was observed in the spectra of the terminal of vibrations W=O groups that were changed from the W–O bond on the surface of WO_3 or in the grain boundaries in WO_3 [38, 39]. Bands at 3380 and 1618 cm^{-1} can be indexed to the $^{-}$OH stretching σ(O–H) bending vibrations of

coordinated water [37]. In the spectra of $Fe_3O_4/Ag_3PO_4@WO_3$ composite, all the characteristic peaks of Fe_3O_4, Ag_3PO_4 and WO_3 are present with a red shift for the peak of Fe_3O_4 (from 579 to 675 cm^{-1}) and blue shift for the peaks of Ag_3PO_4 (from 1028 to 1013 cm^{-1}). The FT-IR analysis further confirms the fabrication of the $Fe_3O_4/Ag_3PO_4@WO_3$ composite.

UV–vis diffuse reflectance spectroscopy and band structure

The study of the light absorption behaviors clearly shows the efficient photocatalytic properties of the semiconductor [40, 41]. The light absorption behaviors of the synthesized photocatalysts were studied by DRS analysis, and the results are shown in (Fig. 7a). The results show that, the light absorptivity of the products shown a trend to increase in the range of 200–520 nm and reached a peak at 510 nm, which belonged to the visible region. The band gap of the synthesized composites was determined by a plot of $(\alpha h\nu)^2$ versus energy (hv), (Fig. 7b). The band gaps were estimated to be 2.42 eV, 2.22 eV and 2.13 eV for WO_3, $Fe_3O_4/Ag_3PO_4@WO_3$ and $Fe_3O_4/Ag_3PO_4@WO_3$-non, respectively. The as synthesized $Fe_3O_4/Ag_3PO_4@WO_3$ composite exhibited the narrower band gap, which is beneficial to its enhanced photocatalytic activity.

Fig. 7 a UV–visible absorption spectra WO_3, $Fe_3O_4/Ag_3PO_4@WO_3$-0.25 mg, $Fe_3O_4/Ag_3PO_4@WO_3$-0.50 and $Fe_3O_4/Ag_3PO_4@WO_3$-0.75 mg and $Fe_3O_4/Ag_3PO_4@WO_3$-0.25 mg-non and **b** plots of $(\alpha h\nu)^2$ versus energy (hv) for the band gap energy of WO3, Fe3O4/Ag3PO4@WO3 and Fe3O4/Ag3PO4@WO3-non

Gasmalla *et al. J Nanobiotechnol*   (2019) 17:58

Page 9 of 14
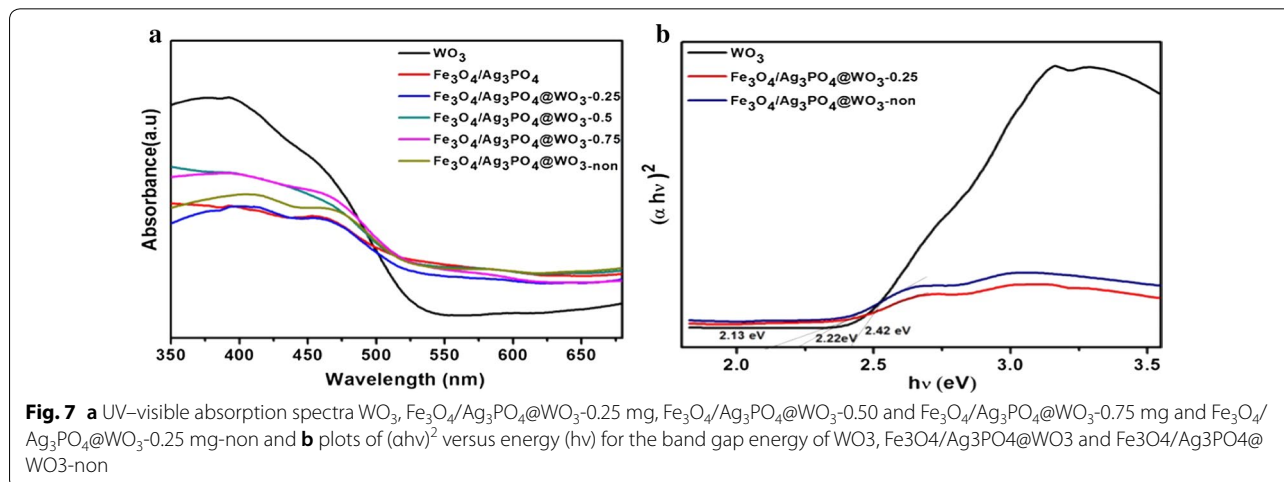
Evaluation of antibacterial activity

Concerning the prospective application of $Fe_3O_4/Ag_3PO_4/WO_3$, the antibacterial properties of the as-synthesized catalyst were investigated in the present work. *S. aureus* even was chosen as representative microorganism. Following the findings above, it was presumed that successful deposition of Ag_3PO_4 imparted antibacterial functions on the nanocomposites [42–44]. To further assess this function, we employed the test method of antimicrobial in term of the inhibitory zone. In a control sample, bacterial colony growth was induced on an Agar dish as illustrated in (Fig. 8a–f), following interfacial contact between the test samples and the Agar plate, which should lead to inhibition of the bacterial growth. The radius of the inhibition zones was measured. As seen in Fig. 8a and c, no bacterial growth inhibition observed in the presence of both Fe_3O_4 and WO_3. The inhibition zone radius for the synthesized composites are ∼13, 19 and 17 mm for Ag_3PO_4, Fe_3O_4/Ag_3PO_4, and $Fe_3O_4/Ag_3PO_4@WO_3$, respectively. Showed that all Ag_3PO_4-based composite has significant bactericidal activity against *S. aureus.* The comparative between $Fe_3O_4/Ag_3PO_4@WO_3$ and $Fe_3O_4/Ag_3PO_4@WO_3$-non composite shows inhibition zone of 12 mm and 17 mm, respectively.
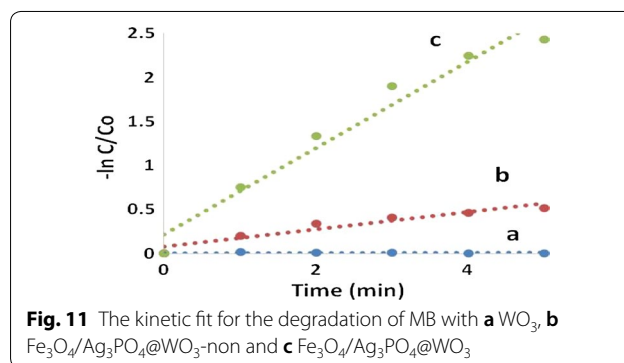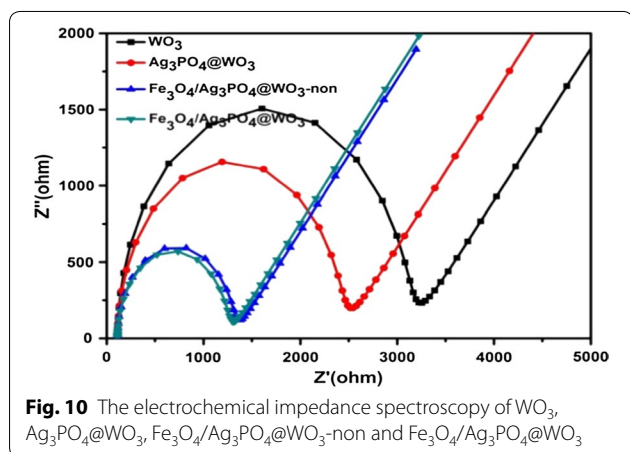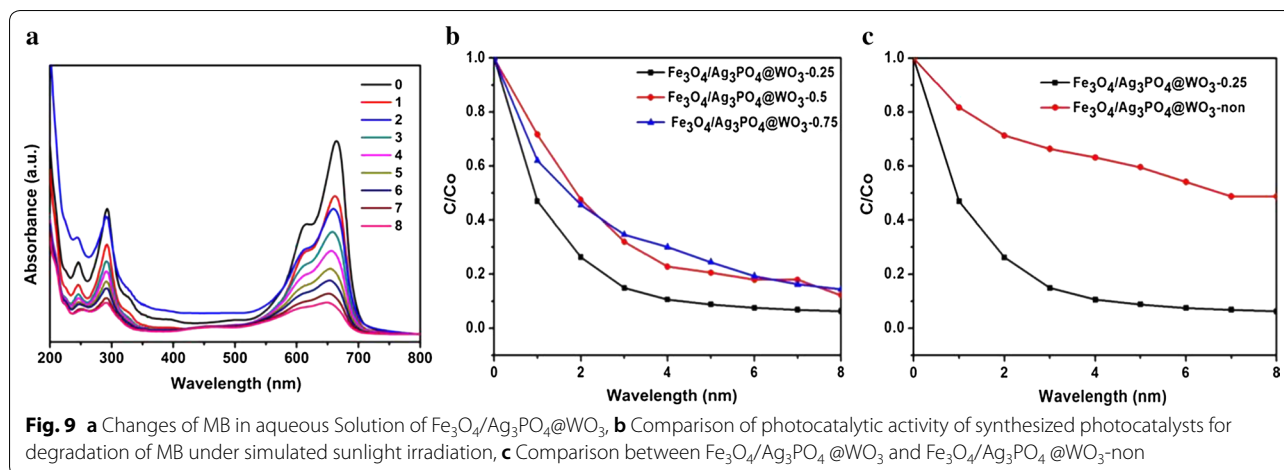
Study of photocatalytic activity

For the evaluation of the photocatalytic activity of the synthesized composites, MB was used as a representative sample. Figure 9a shows the photocatalytic activities of the $Fe_3O_4/Ag_3PO_4@WO_3$ photocatalysts with different ratios of Ag_3PO_4 under simulated light irradiation and the MB solution shows light absorption edge at λ_{max} of 664 nm. In order to investigate the optimum amount of Ag_3PO_4 on the synthesized composite, $Fe_3O_4/Ag_3PO_4@WO_3$ with different Ag_3PO_4 was synthesized, and their photocatalytic activity against MB degradation was studied, and the results are shown in (Fig. 9b). As seen $Fe_3O_4/Ag_3PO_4@WO_3$-0.25 composite, exhibited the higher photocatalytic activity compared with $Fe_3O_4/Ag_3PO_4@WO_3$-0.50 and $Fe_3O_4/Ag_3PO_4@WO_3$-0.75. This is due to the best charge separation and transforming of $Fe_3O_4/Ag_3PO_4@WO_3$-0.25.

To get deeply in the study of the photocatalytic efficiency of $Fe_3O_4/Ag_3PO_4@WO_3$-0.25, its catalytic performance was compared with the $Fe_3O_4/Ag_3PO_4@WO_3$-non
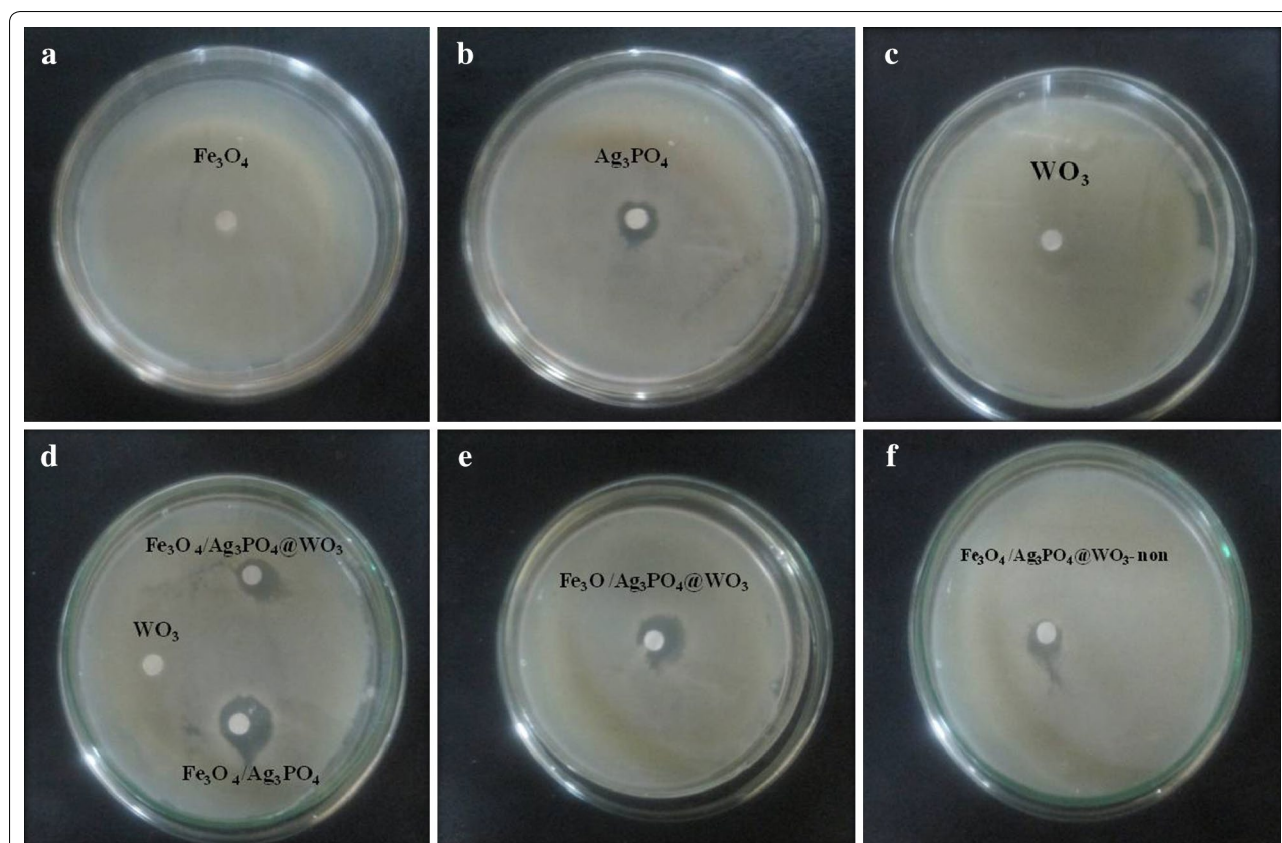
Fig. 8 a–f Images of agar plates containing *S. aureus* after treated by the synthesized composites

Gasmalla *et al. J Nanobiotechnol*   (2019) 17:58

Page 10 of 14

Fig. 9 **a** Changes of MB in aqueous Solution of $Fe_3O_4/Ag_3PO_4@WO_3$, **b** Comparison of photocatalytic activity of synthesized photocatalysts for degradation of MB under simulated sunlight irradiation, **c** Comparison between $Fe_3O_4/Ag_3PO_4@WO_3$ and $Fe_3O_4/Ag_3PO_4@WO_3$-non

Fig. 10 The electrochemical impedance spectroscopy of WO_3, $Ag_3PO_4@WO_3$, $Fe_3O_4/Ag_3PO_4@WO_3$-non and $Fe_3O_4/Ag_3PO_4@WO_3$

Fig. 11 The kinetic fit for the degradation of MB with **a** WO_3, **b** $Fe_3O_4/Ag_3PO_4@WO_3$-non and **c** $Fe_3O_4/Ag_3PO_4@WO_3$

composite. The results are shown in Fig. 9c. As clearly been seen $Fe_3O_4/Ag_3PO_4@WO_3$-0.25 displayed higher photocatalytic activity. 90% of MB degraded within 6 min, while the non-functionalized composite required 8 min to degrade 50% of the dye. The results of the MB degradation revealed that, the $Fe_3O_4/Ag_3PO_4@WO_3$-0.25 composite was exhibited the highest photocatalytic performance. This is because; the functionalization process significantly induced the electron transfer properties of the Fe_3O_4. Therefore, enhanced the electron–hole separation and transfer in the $Fe_3O_4/Ag_3PO_4@WO_3$ composite.

Electrochemical impedance spectroscopy (EIS)
The electrochemical impedance spectroscopy of the WO_3, $Ag_3PO_4@WO_3$, $Fe_3O_4/Ag_3PO_4@WO_3$-non and $Fe_3O_4/Ag_3PO_4@WO_3$ composite was carried out to further investigated the charge transfer and recombination processes in the $Fe_3O_4/Ag_3PO_4@WO_3$ composites under simulated light irradiation, and the result shown in (Fig. 10), a smaller arc radius can be observed on

the EIS Nyquist plot of $Fe_3O_4/Ag_3PO_4@WO_3$-non and $Fe_3O_4/Ag_3PO_4@WO_3$ composite compared with WO_3 and $Ag_3PO_4@WO_3$ indicating that a more effective separation of the photogenerated electron/hole pairs and a faster interfacial charge transfer occurred on the surface of the $Fe_3O_4/Ag_3PO_4@WO_3$ composite.

Kinetic study
In order to investigate the kinetic behavior of the synthesized photocatalysts on the degradation of MB under simulated sunlight irradiation, ln (C/Co) for MB is plotted versus irradiation time according to the following first-order kinetic model 2:

$$\ln(C/Co) = -kt \tag{2}$$

where k is the degradation rate constant, Co and C the initial concentration and the concentration at different irradiation time t of the organic dye respectively. From the result presented in (Fig. 11), the disappearance of MB over the $Fe_3O_4/Ag_3PO_4@WO_3$ synthesized photocatalysts under simulated light irradiation is shown to fit a pseudo first order kinetics pattern, with degradation

Gasmalla *et al. J Nanobiotechnol* (2019) 17:58

Page 11 of 14

rate constants of 0.0018, 0.098 and 0.4906 min^{-1} and R^2: 0.704, 0.918 and 0.959 for WO_3, Fe_3O_4/Ag_3PO_4@WO_3-non and Fe_3O_4/Ag_3PO_4@WO_3 respectively. It is concluded that the degradation of MB over the as-synthesized Fe_3O_4/Ag_3PO_4@WO_3 under light irradiation is five times faster than that of Fe_3O_4/Ag_3PO_4@WO_3-non, indicating the enhanced charge separation in the Fe_3O_4/Ag_3PO_4@WO_3 composite compared with Fe_3O_4/Ag_3PO_4@WO_3-non.

Stability study

The stability of a photocatalyst is important for its practical application. The stability and recyclability of Fe_3O_4/Ag_3PO_4@WO_3 are evaluated by additional experiments to degrade MB under simulated light irradiation cycled for three times. Figure 12a, shows the repeated visible light photocatalytic activity of Fe_3O_4/Ag_3PO_4@WO_3, it can be observed that composite have good stability for the degradation of MB under simulated light irradiation during three cycles.

Active species responsible for MB degradation

The recombination of photogenerated electron–hole pairs is an important limiting factor for the performance of photocatalysts [45, 46]. To study the photocatalytic mechanism of the Fe_3O_4/Ag_3PO_4/WO_{3}0-0.25 composite in detail, the effects of different scavengers on the decomposition of dye molecules were investigated. In order to determined the predominant reactive oxygen species in the photocatalytic process. In this study, *p*-benzoquinone (BZQ), disodium ethylenediamine tetraacetate (Na_2-EDTA) and tert-butanol (t.B) were used as scavengers for $O_2^{\cdot-}$, h^+, and $\cdot OH$, respectively [47]. As seen in (Fig. 12b), the addition of B.Q and t.B has slight effect on the inhibition of the dye degradation. Introducing EDTA to the reaction system the photocatalytic activity

significantly reduced. Which indicate that the photocatalytic reaction mainly depends on the h^+. While $O_2^{\cdot-}$ and $\cdot OH$ have negligible effect. Herein, the highly enhanced photodegradation and antimicrobial activities achieved on Fe_3O_4/Ag_3PO_4@WO_3 can be assigned to its composite structure.

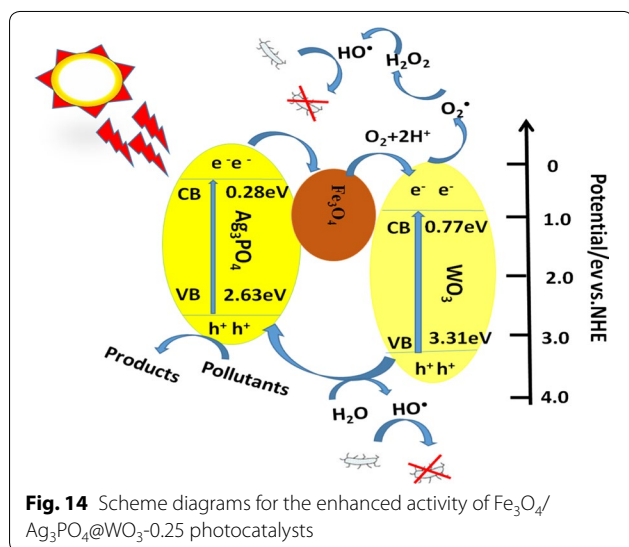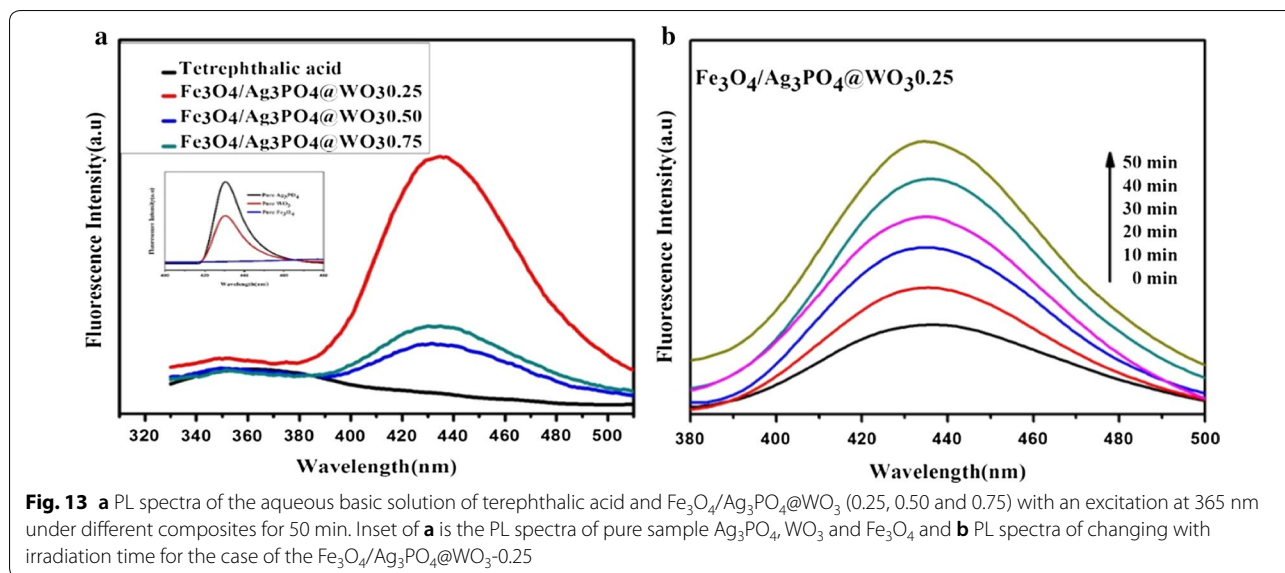The formation of $\cdot OH$ on the surface photo-illuminated of composite Fe_3O_4/Ag_3PO_4@WO_3 (0.25, 0.50 and 0.75) was further confirmed by the PL technique using terephthalic acid as a probe molecule. Figure 13a shows that an obvious difference in PL intensity at about ∼425-430 nm was observed using different catalysts. It was clear that the formation rate of $\cdot OH$ on the Fe_3O_4/Ag_3PO_4@WO_3-0.25 was higher than that of other composite. This implied that the former has higher photocatalytic activity than the latter. Moreover, the inset of (Fig. 13a) the pure Ag_3PO_4 exhibited higher PL intensity than pure WO_3 and pure Fe_3O_4, suggesting that doping of Ag_3PO_4 with WO_3 and Fe_3O_4 was a good route to accelerate the interfacial charge transfer and inhibit the recombination of electron–hole pairs, which resulted in the increase in $\cdot OH$ formation. Moreover, the Fig. 13b depicts the change of PL spectra with irradiation time for the case of Fe_3O_4/Ag_3PO_4@WO_3-0.25. A gradual increase in PL intensity was observed with increasing irradiation time, which suggested that the fluorescence was caused by chemical reactions of terephthalic acid with $\cdot OH$ formed during photo-illuminated reactions. Thus, these results confirmed the evidence of $\cdot OH$ formation and indeed participated in degradation process.

Probable mechanism

As illustrated in Fig. 14 the semiconductors of WO_3 (with an optical band gap of 2.44 eV and Ag_3PO_4 (with an optical band gap of 2.35 eV, especially, the redox potentials (CB and VB) of WO_3 are more positive than
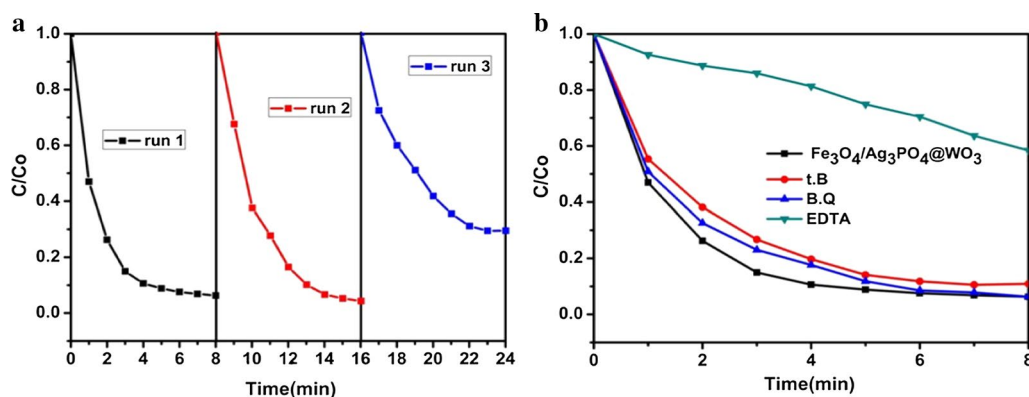
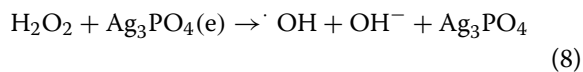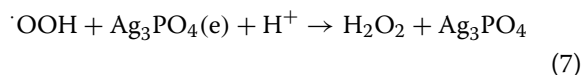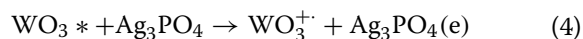**Fig. 12** **a** Stability study on the photocatalytic degradation of MB solution over Fe_3O_4/Ag_3PO_4@WO_3-0.25 nanocomposite under simulated sunlight irradiation, **b** the degradation of MB in the presence of different radical scavengers with Fe_3O_4/Ag_3PO_4 @WO_3 composite

Fig. 13 a PL spectra of the aqueous basic solution of terephthalic acid and $Fe_3O_4/Ag_3PO_4@WO_3$ (0.25, 0.50 and 0.75) with an excitation at 365 nm under different composites for 50 min. Inset of **a** is the PL spectra of pure sample Ag_3PO_4, WO_3 and Fe_3O_4 and **b** PL spectra of changing with irradiation time for the case of the $Fe_3O_4/Ag_3PO_4@WO_3$-0.25

Fig. 14 Scheme diagrams for the enhanced activity of $Fe_3O_4/Ag_3PO_4@WO_3$-0.25 photocatalysts

those of Ag_3PO_4. The electrons from the CB of Ag_3PO_4 can migrate to that of WO_3 and the photogenerated holes could migrate from the VB of WO_3 to that of Ag_3PO_4. The holes could directly oxidize the organic dyes adsorbed on Ag_3PO_4 surface [48–50] and the electrons could be consumed through a multi-electron reaction with oxygen ($O_2 + 2H^+ + 2e^- \rightarrow H_2O_2$, $E^0 = +0.682$ V vs. NHE) [51]. The produced H_2O_2 reacts with an additional electron to produce $\cdot$OH ($H_2O_2 + e^- \rightarrow OH^- + \cdot OH$) [52], which could accelerate the antimicrobial activity.

The major reaction steps in this $Fe_3O_4/Ag_3PO_4@WO_3$ composite photocatalytic mechanism under visible light irradiation are summarized by Eqs. 3–9.

$$WO_3 + h\nu \rightarrow WO_3* \tag{3}$$

$$WO_3 * + Ag_3PO_4 \rightarrow WO_3^{+\cdot} + Ag_3PO_4(e) \tag{4}$$

$$Ag_3PO_4(e) + O_2 \rightarrow Ag_3PO_4 + O_2^{-\cdot} \tag{5}$$

$$O_2^{-\cdot} + H+ \rightarrow \cdot OOH \tag{6}$$

$$\cdot OOH + Ag_3PO_4(e) + H^+ \rightarrow H_2O_2 + Ag_3PO_4 \tag{7}$$

$$H_2O_2 + Ag_3PO_4(e) \rightarrow \cdot OH + OH^- + Ag_3PO_4 \tag{8}$$

Organic pullutant with $\cdot$OH, $O_2^{-\cdot}$ or $H_2O_2 \rightarrow \rightarrow$ (9)

degraded or mineralized products and bacterial activity.

At the same time, the enhanced photocatalytic activity could be expected the composites $Fe_3O_4/Ag_3PO_4/WO_3$-0.25 catalyst due to the effective separation of photogenerated electron–hole pairs. According to the plot of $(Ah\nu)^2$ vs. $h\nu$, the band gaps (E_g) of Ag_3PO_4 and WO_3 are estimated to be 2.35 and 2.44 eV, respectively. The band structure of $Fe_3O_4/Ag_3PO_4/WO_3$ composites can be estimated according to the empirical equations as shown below:

$$VB = X - E^e + 0.5\ E_g \tag{10}$$

$$CB = VB - E_g \tag{11}$$

where EVB and ECB are the valence and conduction band edge potentials, respectively; χ is the electronegativity of the semiconductor; Ee is the energy of free electrons on the hydrogen scale (about 4.5 eV vs. NHE). The χ values for bare Fe_3O_4, Ag_3PO_4 and WO_3 are 5.78, 5.96 and 6.49 eV and, respectively [53–55]. Thus, the EVB of Fe_3O_4, Ag_3PO_4 and WO_3 have been calculated to be 2.18,

2.63 and 3.31 eV vs. NHE, and the corresponding ECB are 0.38, 0.28 and 0.77 eV vs. NHE, respectively.

Conclusions

In this work, novel $Fe_3O_4/Ag_3PO_4@WO_3$ photocatalysts were successfully synthesized via in situ ion-exchange method, and employed in the simulated light degradation of organic contaminants (Methylene Blue). The as synthesized composite exhibited enhanced photocatalytic activity compared with $Fe_3O_4/Ag_3PO_4@WO_3$-non and the bare WO_3. In addition, the effect of the Ag_3PO_4 amount on the photocatalytic activity of the $Fe_3O_4/Ag_3PO_4@WO_3$ was investigated. The $Fe_3O_4/Ag_3PO_4@WO_3$-0.25 exhibited the higher photocatalytic activity. The antibacterial behaviors of the synthesized composite were studied. All the Ag_3PO_4, Fe_3O_4/Ag_3PO_4 and $Fe_3O_4/Ag_3PO_4@WO_3$ based composites exhibited enhancement in bactericidal efficiency. The oleic acid functionalized composite $Fe_3O_4/Ag_3PO_4@WO_3$ also exhibited the high inhibition zone. The reactive species trapping study revealed that, the hole played the main role on the photocatalytic activity enhancement.

Authors' contributions

HBG: carried all most experiment and write the paper, MIS: participate of the analysis of photocatalyst data, ANC: participated in experiment of active species of photocatalyst and XQL, GWD and LBN: supervision guidance and participation in the manuscript drafted and correction the language. All authors read and approved the final manuscript.

Author details

[1] Key Laboratory of Environmental Materials & Environmental Engineering of Jiangsu Province, College of Chemistry and Chemistry Engineering, Yangzhou University, Yangzhou 225002, China. [2] Forest Products and Industries Department, Faculty of Forestry, University of Khartoum, Khartoum, Sudan. [3] Key Laboratory of Bioelectrochemistry & Environmental Analysis of Gansu Province, College of Chemistry & Chemical Engineering, Northwest Normal University, Lanzhou 730070, China. [4] Chemistry Department, Faculty of Science, International University of Africa, Khartoum, Sudan.

Competing interests

The authors declare that they have no competing interests.

Availability of data and materials

Not applicable.

Consent for publication

The manuscript is not under consideration for publication elsewhere.

Ethics approval and consent to participate

Not applicable.

Publisher's Note

Springer Nature remains neutral with regard to jurisdictional claims in published maps and institutional affiliations.

References

1. Sclafani A, Palmisano L, Schiavello M. Influence of the preparation methods of TiO sub 2 on the photocatalytic degradation of phenol in aqueous dispersion. J Phys Chem USA. 1990;94(2):829–32.
2. Sato J, Kobayashi H, Ikarashi K, Saito N, Nishiyama H, Inoue Y. Photocatalytic activity for water decomposition of RuO2-dispersed Zn2GeO4 with d10 configuration. J Phys Chem B. 2004;108(14):4369–75.
3. Bagheri S, Julkapli NM. Magnetite hybrid photocatalysis: advance environmental remediation. Rev Inorg Chem. 2016;36(3):135–51.
4. Cheng X-L, Jiang J-S, Jin C-Y, Lin C-C, Zeng Y, Zhang Q-H. Cauliflower-like α-Fe 2 O 3 microstructures: toluene–water interface-assisted synthesis, characterization, and applications in wastewater treatment and visible-light photocatalysis. Chem Eng J. 2014;236:139–48.
5. Martinez DS, Martínez-De La Cruz A, Cuéllar EL. Photocatalytic properties of WO 3 nanoparticles obtained by precipitation in presence of urea as complexing agent. Appl Catal A. 2011;398(1):179–86.
6. Sun J, Chen G, Wu J, Dong H, Xiong G. Bismuth vanadate hollow spheres: bubble template synthesis and enhanced photocatalytic properties for photodegradation. Appl Catal B. 2013;132:304–14.
7. Zhang F-J, Xie F-Z, Liu J, Zhao W, Zhang K. Rapid sonochemical synthesis of irregular nanolaminar-like Bi 2 WO 6 as efficient visible-light-active photocatalysts. Ultrason Sonochem. 2013;20(1):209–15.
8. Bi Y, Ouyang S, Umezawa N, Cao J, Ye J. Facet effect of single-crystalline Ag3PO4 sub-microcrystals on photocatalytic properties. J Am Chem Soc. 2011;133(17):6490–2.
9. Kang YS, Risbud S, Rabolt JF, Stroeve P. Synthesis and characterization of nanometer-size Fe3O4 and γ-Fe2O3 particles. Chem Mater. 1996;8(9):2209–11.
10. Wang Y, Li S, Xing X, Huang F, Shen Y, Xie A, Wang X, Zhang J. Self-assembled 3D flowerlike hierarchical Fe3O4@ Bi2O3 core–shell architectures and their enhanced photocatalytic activity under visible light. Chem A Eur J. 2011;17(17):4802–8.
11. Xu J-W, Gao Z-D, Han K, Liu Y, Song Y-Y. Synthesis of magnetically separable Ag3PO4/TiO2/Fe3O4 heterostructure with enhanced photocatalytic performance under visible light for photoinactivation of bacteria. ACS Appl Mater Interfaces. 2014;6(17):15122–31.
12. Wu A, Tian C, Chang W, Hong Y, Zhang Q, Qu Y, Fu H. Morphology-controlled synthesis of Ag 3 PO 4 nano/microcrystals and their antibacterial properties. Mater Res Bull. 2013;48(9):3043–8.
13. Liu J-K, Luo C-X, Wang J-D, Yang X-H, Zhong X-H. Controlled synthesis of silver phosphate crystals with high photocatalytic activity and bacteriostatic activity. CrystEngComm. 2012;14(24):8714–21.
14. Li G, Mao L. Magnetically separable Fe 3 O 4–Ag 3 PO 4 sub-micrometre composite: facile synthesis, high visible light-driven photocatalytic efficiency, and good recyclability. RSC Adv. 2012;2(12):5108–11.
15. Patil SS, Tamboli MS, Deonikar VG, Umarji GG, Ambekar JD, Kulkarni MV, Kolekar SS, Kale BB, Patil DR. Magnetically separable Ag 3 PO 4/NiFe 2 O 4 composites with enhanced photocatalytic activity. Dalton Trans. 2015;44(47):20426–34.
16. Sun J, Fan H, Nan B, Ai S. Fe3O4@ LDH@ Ag/Ag3PO4 submicrosphere as a magnetically separable visible-light photocatalyst. Sep Purif Technol. 2014;130:84–90.
17. Yao YR, Huang WZ, Zhou H, Cui X, Zheng YF, Song XC. Synthesis of core–shell nanostructured magnetic photocatalyst Fe 3 O 4@ SiO 2@ Ag

3 PO 4 with excellent visible-light-responding photocatalytic activity. J Nanoparticle Res. 2014;16(11):2742.

18. Guo X, Chen N, Feng C, Yang Y, Zhang B, Wang G, Zhang Z. Performance of magnetically recoverable core–shell Fe3O4@ Ag3PO4/AgCl for photocatalytic removal of methylene blue under simulated solar light. Catal Commun. 2013;38:26–30.

19. Miseki Y, Kusama H, Sugihara H, Sayama K. Cs-modified WO3 photocatalyst showing efficient solar energy conversion for O2 production and Fe(III) ion reduction under visible light. J Phys Chem Lett. 2010;1(8):1196–200.

20. Liu Z, Zhao Z-G, Miyauchi M. Efficient visible light active CaFe2O4/WO3 based composite photocatalysts: effect of interfacial modification. J Phys Chem C. 2009;113(39):17132–7.

21. Seifollahi Bazarjani M, Hojamberdiev M, Morita K, Zhu G, Cherkashinin G, Fasel C, Herrmann T, Breitzke H, Gurlo A, Riedel R. Visible light photocatalysis with c-WO3−x/WO3 × H2O nanoheterostructures in situ formed in mesoporous polycarbosilane-siloxane polymer. J Am Chem Soc. 2013;135(11):4467–75.

22. Zhang G, Wang W, Li X. Enhanced thermoelectric properties of core/shell heterostructure nanowire composites. Adv Mater. 2008;20(19):3654–6.

23. Sun X, Li Y. Colloidal carbon spheres and their core/shell structures with noble-metal nanoparticles. Angew Chem Int Ed. 2004;43(5):597–601.

24. Subramanian V, Wolf EE, Kamat PV. Catalysis with TiO2/gold nanocomposites. Effect of metal particle size on the Fermi level equilibration. J Am Chem Soc. 2004;126(15):4943–50.

25. Formo E, Lee E, Campbell D, Xia Y. Functionalization of electrospun TiO2 nanofibers with Pt nanoparticles and nanowires for catalytic applications. Nano Lett. 2008;8(2):668–72.

26. Awazu K, Fujimaki M, Rockstuhl C, Tominaga J, Murakami H, Ohki Y, Yoshida N, Watanabe T. A plasmonic photocatalyst consisting of silver nanoparticles embedded in titanium dioxide. J Am Chem Soc. 2008;130(5):1676–80.

27. Wu W, Jiang C, Roy VA. Recent progress in magnetic iron oxide–semiconductor composite nanomaterials as promising photocatalysts. Nanoscale. 2015;7(1):38–58.

28. Xi G, Yue B, Cao J, Ye J. Fe3O4/WO3 hierarchical core–shell structure: high-performance and recyclable visible-light photocatalysis. Chem A Eur J. 2011;17(18):5145–54.

29. Zhou M, Lou XWD, Xie Y. Two-dimensional nanosheets for photoelectrochemical water splitting: possibilities and opportunities. Nano Today. 2013;8(6):598–618.

30. Sin J-C, Lam S-M, Lee K-T, Mohamed AR. Photocatalytic performance of novel samarium-doped spherical-like ZnO hierarchical nanostructures under visible light irradiation for 2, 4-dichlorophenol degradation. J Colloid Interface Sci. 2013;401:40–9.

31. Yu J, Wang W, Cheng B, Su B-L. Enhancement of photocatalytic activity of mesporous TiO2 powders by hydrothermal surface fluorination treatment. J Phys Chem C. 2009;113(16):6743–50.

32. Zhang W, Shi X, Huang J, Zhang Y, Wu Z, Xian Y. Bacitracin-conjugated superparamagnetic iron oxide nanoparticles: synthesis, characterization and antibacterial activity. Chemphyschem. 2012;13(14):3388–96.

33. Wang J-D, Liu J-K, Luo C-X, Yang X-H. Light-dependent controlled synthesis and photocatalytic properties of stable Ag 3 nanocrystals. Mater Res Bull. 2014;60:783–93.

34. Bi Y, Hu H, Ouyang S, Jiao Z, Lu G, Ye J. Selective growth of metallic Ag nanocrystals on Ag3PO4 submicro-cubes for photocatalytic applications. Chem A Eur J. 2012;18(45):14272–5.

35. Ghosh S, Acharyya SS, Sasaki T, Bal R. Room temperature selective oxidation of aniline to azoxybenzene over a silver supported tungsten oxide nanostructured catalyst. Green Chem. 2015;17(3):1867–76.

36. Mohite S, Rajpure K. Synthesis and characterization of Sb doped ZnO thin films for photodetector application. Opt Mater. 2014;36(4):833–8.

37. Nogueira HI, Cavaleiro AM, Rocha J, Trindade T, de Jesus JDP. Synthesis and characterization of tungsten trioxide powders prepared from tungstic acids. Mater Res Bull. 2004;39(4):683–93.

38. Daniel M, Desbat B, Lassegues J, Gerand B, Figlarz M. Infrared and Raman study of WO3 tungsten trioxides and WO3, xH2O tungsten trioxide tydrates. J Solid State Chem. 1987;67(2):235–47.

39. Díaz-Reyes J, Dorantes-García V, Pérez-Benítez A, Balderas-López J. Obtaining of films of tungsten trioxide (WO3) by resistive heating of a tungsten filament. Superficies y vacío. 2008;21(2):12–7.

40. Alamri SN. Study of thermocolored WO3 thin film under direct solar radiation. Smart Mater Struct. 2009;18(2):025010.

41. Yi Z, Ye J, Kikugawa N, Kako T, Ouyang S, Stuart-Williams H, Yang H, Cao J, Luo W, Li Z. An orthophosphate semiconductor with photooxidation properties under visible-light irradiation. Nat Mater. 2010;9(7):559–64.

42. Zhao G, Stevens SE. Multiple parameters for the comprehensive evaluation of the susceptibility of *Escherichia coli* to the silver ion. Biometals. 1998;11(1):27–32.

43. Yamanaka M, Hara K, Kudo J. Bactericidal actions of a silver ion solution on *Escherichia coli*, studied by energy-filtering transmission electron microscopy and proteomic analysis. Appl Environ Microbiol. 2005;71(11):7589–93.

44. Jung WK, Koo HC, Kim KW, Shin S, Kim SH, Park YH. Antibacterial activity and mechanism of action of the silver ion in *Staphylococcus aureus* and *Escherichia coli*. Appl Environ Microbiol. 2008;74(7):2171–8.

45. Wu K, Zhu H, Liu Z, Rodríguez-Córdoba W, Lian T. Ultrafast charge separation and long-lived charge separated state in photocatalytic CdS–Pt nanorod heterostructures. J Am Chem Soc. 2012;134(25):10337–40.

46. Yu J, Ma T, Liu S. Enhanced photocatalytic activity of mesoporous TiO 2 aggregates by embedding carbon nanotubes as electron-transfer channel. Phys Chem Chem Phys. 2011;13(8):3491–501.

47. Tang J, Liu Y, Li H, Tan Z, Li D. A novel Ag 3 AsO 4 visible-light-responsive photocatalyst: facile synthesis and exceptional photocatalytic performance. Chem Commun. 2013;49(48):5498–500.

48. Katsumata H, Taniguchi M, Kaneco S, Suzuki T. Photocatalytic degradation of bisphenol A by Ag 3 PO 4 under visible light. Catal Commun. 2013;34:30–4.

49. Kumar S, Surendar T, Baruah A, Shanker V. Synthesis of a novel and stable gC 3 N 4–Ag 3 PO 4 hybrid nanocomposite photocatalyst and study of the photocatalytic activity under visible light irradiation. J Mater Chem A. 2013;1(17):5333–40.

50. Xu Y-S, Zhang W-D. Monodispersed Ag 3 PO 4 nanocrystals loaded on the surface of spherical Bi 2 MoO 6 with enhanced photocatalytic performance. Dalton Trans. 2013;42(4):1094–101.

51. Rawal SB, Do Sung S, Lee WI. Novel Ag 3 PO 4/TiO 2 composites for efficient decomposition of gaseous 2-propanol under visible-light irradiation. Catal Commun. 2012;17:131–5.

52. Kim J, Lee CW, Choi W. Platinized WO3 as an environmental photocatalyst that generates OH radicals under visible light. Environ Sci Technol. 2010;44(17):6849–54.

53. Katsumata H, Sakai T, Suzuki T, Kaneco S. Highly efficient photocatalytic activity of g-C3N4/Ag3PO4 hybrid photocatalysts through Z-scheme photocatalytic mechanism under visible light. Ind Eng Chem Res. 2014;53(19):8018–25.

54. Chen S, Hu Y, Meng S, Fu X. Study on the separation mechanisms of photogenerated electrons and holes for composite photocatalysts gC 3 N 4-WO 3. Appl Catal B. 2014;150:564–73.

55. Xu Y, Schoonen MA. The absolute energy positions of conduction and valence bands of selected semiconducting minerals. Am Miner. 2000;85(3–4):543–56.